DYNAMICS OF A VERTICAL TAKEOFF AND LANDING (VTOL) UNMANNED AERIAL VEHICLE (UAV)

Alvaro Vargas-Clara, Arizona State University; Sangram Redkar, Arizona state University

Abstract

The objective of this work was to develop a stop-rotor unmanned aerial vehicle (UAV). This UAV would be capable of vertical takeoff and landing like a helicopter and could convert from a helicopter mode to an airplane mode in mid-flight. Thus, this UAV could hover as a helicopter and achieve high mission range like an airplane. The term stop-rotor implies that in midflight the lift generating helicopter rotor stops and the rotor blades transform into airplane wings. The thrust in the airplane mode is provided by a pusher propeller. This aircraft configuration presented unique challenges in modeling, aerodynamics, and control. Another important task was to design an autopilot for this configuration that would stabilize the aircraft and allow it to operate in a fly-by–wire mode. In this paper presented the modeling and aircraft design along with a brief discussion of the autopilot architecture of this UAV. Also presented are some experimental "conversion" results, where a stop-rotor aircraft was dropped from a hot-air balloon and performed successful conversions from helicopter to airplane mode and vice versa.

Introduction

For any meaningful payload, speed, or endurance, airplanes need runways. Helicopters, having no need for runways, cannot compare with their fixed-wing relatives for payload, speed, range, or endurance. A vehicle that would not require a runway like a helicopter but enjoy the payload, speed, range, and endurance of an airplane would be an ideal aircraft. The multimode rotors on tilt-rotor vehicles, such as the V-22 Osprey and the TR911D Eagle Eye UAV, are compromised in terms of factors such as blade twist and geometry, due to conflicting requirements depending on the mode of flight. While cruising as a fixed–wing machine, the rotors are far from ideal as a thrust device; and while in helicopter mode, the rotors are likewise far from ideal in the hover mode and particularly in autorotation. Such fundamental compromises will likely make a candidate tilt-rotor small VTOL UAV performance fall well short of the mission range and endurance performance objectives over fixed-wing aircraft (citing the Scan Eagle example) and gain the VTOL capability. For over five decades, the aerospace community has recognized that such an ideal aircraft would likely be of a stop-rotor configuration. For most of those five decades, innumerable stop-rotor concepts and ideas have been advanced. Among recent efforts have been the cancelled Boeing X-50 Canard Rotor Wing and the Sikorsky X-Wing.

In virtually every case known to the authors, the stop-rotor concepts were of a radial-flow conversion category. This is to say the rotor disc is parallel to the airflow during conversion when the rotors are to be slowed and stopped to become wings. Like the critical roll-control issue plaguing airplane developers fifty years since Cayley's experiments, the stop-rotor development progress has been stalled for fifty years mainly over the obstacle of the conversion approach between rotary and fixed-wing modes of flight. What is demonstrably needed in order to resolve this critical issue from hampering stop-rotor development is a departure from the radial-flow conversion approach. A stop-rotor proposed here is the first and only stop-rotor concept where an axial-flow conversion approach is advanced. Axial-flow conversion is analogous to feathering or pitching propellers with the airflow impinging upon the rotor disc plane perpendicularly, aligned with the rotational axis of the rotor. The principal advantage of an axial-flow conversion approach compared to the radial-flow conversion is that the airflow impinging the airfoil does not change direction; as such, the airfoil can have conventional, normal profiles with aero-elastically-stable quarter-chord pitch axes.

The flight Conversion Concept for the stop-rotor is illustrated in Figure 1. It is important to note that the stop-rotor craft can convert between helicopter and airplane modes of flight any number of times during the same flight. The helicopter mode is not just the launch and recovery method that some have misunderstood from this illustration. Really, the point of this illustration is to emphasize the conversion sequence between helicopter and airplane mode of flight for the vehicle.

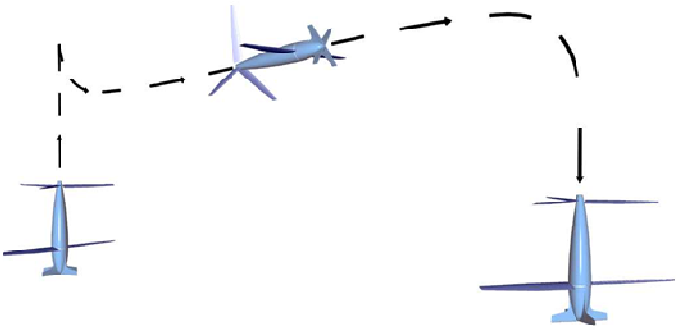

Figure 1. Stop-Rotor Flight Conversion

For example, from the powered helicopter mode, a selectable clutch is released while the wings and tail fins are collectively pitched (analogous to feathering a propeller) until in the airplane-mode position. The wings and tail fins stop rotation solely due to external aerodynamic forces and do not require indexing or braking and/or a locking mechanism of any kind. The selectable clutch engages the propeller drive shaft so that power can be delivered to the pusher propeller for the airplane-mode of flight. The propeller is thus optimized for cruising and not compromised like many other fixed-pitch propeller UAVs for take-off and cruise conditions. In the conversion from airplane to helicopter (from powered airplane) mode, the clutch is released and the wing and tailfins are collectively pitched to the autorotation position. The wings and tail fins spin up solely due to external aerodynamic forces. The selectable clutch engages the tail fin hub and power is then delivered to the tail fin for powered helicopter mode of flight while the collective pitch is increased to provide hovering and normal helicopter-like flight in the usual manner. Thus, the stop-rotor design is an ideal fixed-wing, uncompromised in terms of propulsion and landing mechanism making available higher weight fractions for payload and fuel for longer endurance and greater payload than conventional fixed-wing designs. In helicopter mode, the stop-rotor craft is an ideal rotary-wing vehicle, with efficient, slow turning rotors without a power-robbing tail rotor for anti-torque.

Mathematical Modeling of the Stop-Rotor UAV

Consider the stop-rotor configuration of Figure 2. In order to develop the mathematical model, the stop-rotor structure is divided into the following subcomponents.

a) Tail rotor: The tail rotor is comprised of three identical tail fins. It acts as a rotor in the helicopter mode and generates lift.
b) Wings: The wings provide the lift in the airplane mode and have control surfaces. In the helicopter mode, the wings rotate due to torque reaction.
c) Fuselage: The fuselage houses the electro-optical payload and is stationary during helicopter or aircraft mode.

In this section, the mathematical model of the stop-rotor design is briefly discussed. This model is incorporated in the MATLAB code. The mathematical model is developed using d'Alembert's principle considering dynamic, gravity, and aerodynamic forces [1-3]. For the initial analysis, the stop-rotor tail rotor is assumed to be unpowered and conversion from helicopter mode to airplane mode is achieved by feathering the wings. The following coordinate systems are used to develop the model as shown in Figure 2.

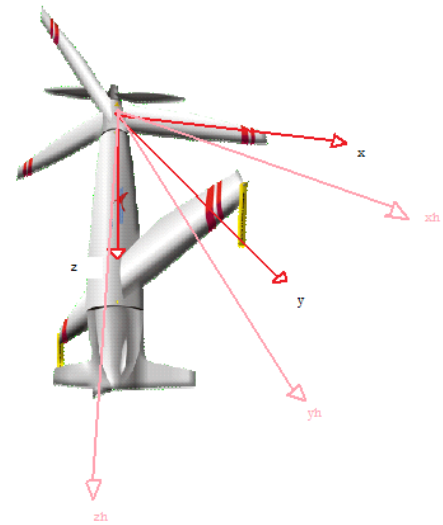

Figure 2. Stop-Rotor Configuration and Coordinate Axes

1. Tail rotor body fixed coordinate system that rotates with tail rotor.
2. Hub coordinate system coinciding with the tail-rotor coordinate system but fixed to hub.
3. Wing coordinate system: wing fixed coordinate system rotating with wing in the helicopter mode.
4. Gravity coordinate system: located on fuselage coinciding with the hub coordinate system but z axis is always pointed downwards aligning itself with the pull of gravity.
5. Ground coordinate system inertial coordinate system located fixed on ground.

In this study, procedures for deriving the equations of motion were similar to those of other studies [1-3]. The gravity coordinate system is translated from the ground coordinate system with $\mathbf{x} = [x_G, y_G, z_G]$; where x_G, y_G, z_G corresponds to distances from the inertial reference frame. The relation between the coordinates in both the systems is given by

$$\mathbf{x}_p = \mathbf{A}(\psi, \theta, \phi)\mathbf{x} \tag{1}$$

where $\mathbf{A}(\psi, \theta, \phi)$ is the generalized rotation matrix and ψ, θ, ϕ are inertial yaw, pitch and roll angles. Equations of motion for the stop-rotor configuration are grouped as

$$\begin{aligned} \mathbf{F}_{TR} + \mathbf{F}_F + \mathbf{F}_W &= 0 \\ \mathbf{M}_{TR} + \mathbf{M}_W + \mathbf{M}_W &= 0 \end{aligned} \tag{2}$$

where $\mathbf{F}_{TR}, \mathbf{F}_F, \mathbf{F}_W$ are the forces acting on the tail rotor, fuselage and wings, and $\mathbf{M}_{TR}, \mathbf{M}_W, \mathbf{M}_W$ are the moments acting on the tail rotor, fuselage and wings. Each element of Equation (2) is comprised of inertia, aerodynamic and gravity parts.

Inertial Loads: The expressions for inertial load, $\mathbf{Q}_{pi}$, is obtained using the conservation of momentum, which can be written in the general form as

$$\mathbf{Q}_{pi} = \mathbf{I}_{pi}(\dot{\mathbf{Y}}_{pi} + \dot{\mathbf{Y}}_{mi}) + (\mathbf{\Omega}_{pi} + \mathbf{\Omega}_{mi})\mathbf{I}_{pi}(\mathbf{Y}_{pi} + \mathbf{Y}_{mi}) \quad (3)$$

where $\mathbf{I}_{pi}$ is the generalized inertia matrix, $\mathbf{Y}_{pi}$ is the state vector comprising the components of velocities and rates. $\mathbf{Y}_{mi}$ is the state vector comprising the relative velocities and rates. $\mathbf{\Omega}_{pi}, \mathbf{\Omega}_{mi}$ are angular velocities and relative angular velocity matrices. The nonlinear parts of Equation (3) contains all acceleration acting on the rotating elements including gyroscopic effects.

Gravity Loads: The vector of gravity acceleration in the gravity coordinate system is given by $\mathbf{g} = [0, 0, g]^T$. The gravity vector can be rotated using the transformation matrix $\mathbf{A}_G(\psi, \theta, \phi)$. The gravity loads on stop-rotor components can be calculated as

$$\begin{aligned} \mathbf{F}_{ig} &= m_i \mathbf{A}_G \mathbf{g} \\ \mathbf{M}_{ig} &= \mathbf{r}_{CG} \times (m_i \mathbf{A}_G \mathbf{g}) \end{aligned} \quad (4)$$

where m_i is the mass of the element/component and $\mathbf{r}_{CG}$ is the position vector from the center of gravity of the element relative to the reference coordinate frame.

Aerodynamic Loads: The differential aerodynamic loads comprising drag, lift and moment on element i, can be expressed in the element coordinate system as

$$\begin{aligned} dD &= \frac{1}{2}\rho c(y) V_a^2 C_D(\alpha) dy \\ dL &= \frac{1}{2}\rho c(y) V_a^2 C_L(\alpha) dy \\ dM &= \frac{1}{2}\rho c^2(y) V_a^2 C_M(\alpha) dy \end{aligned} \quad (5)$$

where $\frac{1}{2}\rho V_a^2$ is the dynamic pressure and $C_D(\alpha), C_L(\alpha), C_M(\alpha)$ are coefficients of drag, lift and moment, respectively. The aerodynamic forces in the element coordinate system can be transformed to the coordinate system corresponding to Equation (2). It is important to note that the tail fin and wing has NACA0012 airfoil, which is widely studied and performance data is available in the literature. However, to characterize fuselage aerodynamic coefficients, CFD modeling, and/or wind-tunnel testing is required.

Design Considerations

In the course of detailed design, Finite Element (FE) Analysis was used. In this section, aerodynamic and FE analysis on the stop-rotor wing is briefly presented [4]. A wing under operating conditions experiences aerodynamic loads. These aerodynamic loads were used to conduct a structural analysis on the wing. The wing was modeled as pin supported at two bearing locations at aluminum spar. The loads that the wing structure experienced were lift force, drag force, and moment. All aerodynamic loads were assumed to be acting at a quarter-chord point and to be constant along the span of the wing.

The first step in conducting this analysis was to determine the aerodynamic loads that the wing structure would experience. These loads were determined by conducting a 2D CFD analysis on a NACA 0012 airfoil. The calculated Reynolds number at which the wing would operate was 483,908 at STP. The CFD analysis was conducted using XFLR 5 [5] software. In doing the CFD analysis, coefficients of lift, drag, and moment were obtained (shown in Tables 1 and 2) at various angles of attack (alpha).

Table 1. Coefficient of Lift, Drag and Moment at Different Angles of Attack [4]

Alpha	CL	CD	CM
0	0	0.00623	0
5	0.6317	0.01049	-0.0134
10	1.0411	0.01955	0.0114
15	1.2194	0.04987	0.0331

Once these coefficients were obtained, the aerodynamic forces were calculated using Equation (5).

Table 2: Aerodynamic Loads at Different Angles of Attack [4]

Alpha	Lift per unit Span(N/m)	Drag per unit Span (N/m)	Moment per unit Span(Nm)
0	0	0.7196791	0
5	72.97292	1.2117871	-0.41284
10	120.2661	2.2583831	0.35122
15	140.863	5.7608984	1.019769

The next step was to construct the wing structure using Solidworks [6]. The structure is shown in Figure 3 and consists of two major components: an airfoil skin and the aluminum spar. The span of the wing was 47.5 inches and the thickness was assumed to be 0.1 inches. The aluminum spar had a span of 52.5 inches and the thickness of the aluminum spar was measured to be 0.125 inches. The material for both components was assumed to be Aluminum 2014.

The wing structure was then inputted into NX 7 Nastran [7], where mesh, constraints, and loads were applied. The elements selected for this analysis were thin-shell Quad-4, and solid Hex-8. The airfoil skin used the thin shell, while the aluminum spar used solid elements. A 2D mapped mesh was applied on the airfoil skin, while a 3D swept mesh was applied on the aluminum cross-section. This resulted in a uniform mesh in the aluminum spar and airfoil, as shown in

Figure 3. A face split was used on the top surface of the airfoil to create a single contact point with the aluminum spar. At this location, the spar and airfoil shared common nodes along the span-wise direction.

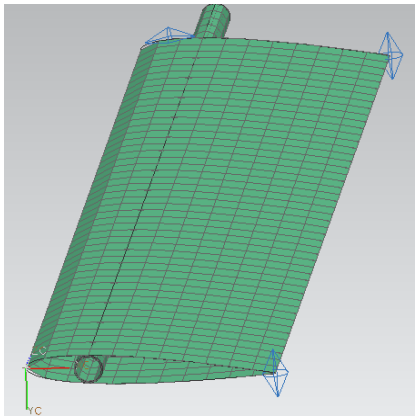

Figure 3. Wing structure and FE mesh. [2]

The last step in setting up the analysis was to input the loads and constraints. The edge created by the face split was used to apply the lift and drag forces. The lift force was applied on the top surface of the airfoil skin in the negative y-direction, while the drag force was split in half and applied to the top and bottom of the spar in the x-direction. The moment was applied to the inner surface of the tube in the z-direction. The constraints used for this analysis were pinned constraints at the aluminum spar. These constraints were selected to simulate the mounting structure of the wing. The method of applying these constraints was using a user-defined constraint. This was done by fixing the translations in the x, y, and z directions for selected nodes at the locations where the bearing supports would be located.

For this structural analysis, the results obtained were for deflection, Von Mises stresses, and vibration of the wing structure. This analysis was conducted using the maximum values of lift, drag, and moment forces previously obtained. The wing structure had a maximum magnitude deflection of 0.167 inches located at the tip of the wing (as shown in Figure 4). The minimum deflection was 0 inches, situated at the constraints.

The maximum and minimum deflections in the x and y directions are given in Table 3:

Table 3. Maximum and Minimum Deflection in x and y Directions [4]

Direction	Maximum	Minimum
X-direction	0.002243 in.	-0.00029 in.
Y-direction	0.1672 in.	-0.00675 in.

The maximum Von-Mises stress was found to be 5,421 psi located next to the pinned constraint, while the minimum Von-Mises stress was 1.931 psi at the tip of wing. These results are presented in Figure 5.

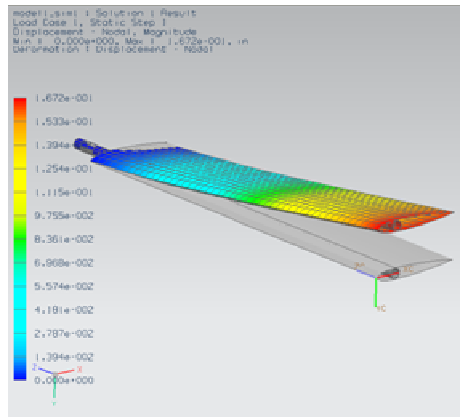

Figure 4: Magnitude Deflection of wing structure [4].

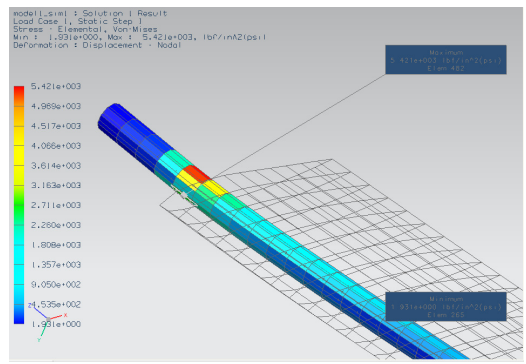

Figure 5. Von Mises Stress in entire wing structure [4]

The maximum Von-Mises stress occurred at the bottom and top of the spar right after the constraints; this is understandable since the wing structure is mostly experiencing a bending due to the lift. As well, the maximum stress of 5,421 psi is well within the yield strength of Aluminum 2014, which is 60,000 psi. This relatively low Von-Mises value is due to the weak loading conditions the structure experienced. The aerodynamic forces were calculated using the assumption that the maximum velocity the wing would experience would be 26.82m/s, which is a qualified small velocity. So, the aerodynamic forces were small. The results obtained from vibration are realistic because they illustrated all of the deformations that are expected under vibration. The stop-rotor wing exhibits the following modes, as shown in Table 4. These modes are depicted in Figure 6.

Table 4: Vibration Deformations [4]

Vibration Frequency	Deformation Type
Mode 1: 15.9 Hz	Bending
Mode 2: 19.6 Hz	Lead or Drag
Mode 3: 71 Hz	Torsion
Mode 4: 112.5 Hz	Second Bending

Mode 5: 168.3 Hz	Second Torsion

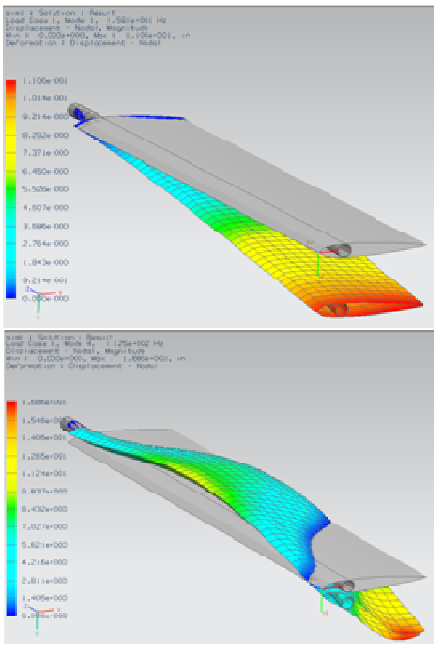

Figure 6: Stop-Rotor Wing Vibration Modes [2]

Airframe Fabrication and Autopilot

After design validation, a test stand and airframe was fabricated in collaboration with local industry, as shown in Figure 7.

Figure 7: Stop-Rotor Test Stand

Collective feathering of the wing is the most important aspect of this design that enables the aircraft to transition from rotary-wing to fixed-wing configuration and vice versa. The wing collective control is obtained by two independent motor controllers. Each controller is powered by a separate battery pack. An RC interface is provided for collective and aileron control.

In order to log the data from the test instrumentation based on an open-source autopilot, Ardupilot was used [8]. This instrumentation is comprised of an autopilot that has static and pitot pressure sensors, thermopiles and GPS. This autopilot used in the data-logging mode, along with Zigbee wireless transmitter and receiver, and a ground station, is shown in Figure 8. It is anticipated that this instrumentation will later be used as an autopilot for the stop-rotor UAV.

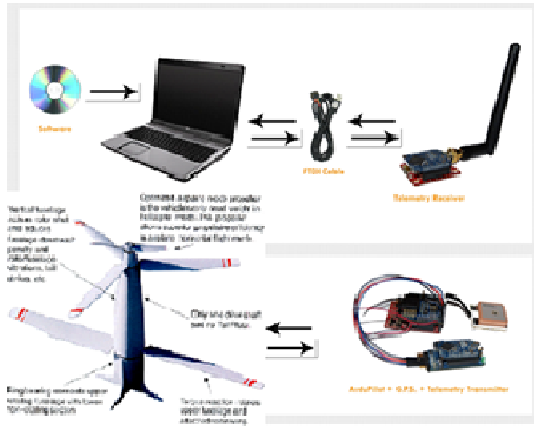

Figure 8. Ardupilot [8] Interface for the Stop-Rotor Design

The ground station interface was implemented using open-source software [8]. However, the Labview interface was modified to incorporate data-logging capability, as shown in Figure 9. This ground station interface shows airspeed, GPS location, attitude, and altitude of the aircraft.

Figure 9. Ground Station Interface for Stop-Rotor [8]

Experimental Validation of Stop-Rotor Conversion

In order to demonstrate the conversion, a "big drop" test was scheduled. In this drop test, an unpowered stop-rotor test specimen was dropped from a hot-air balloon with the wings and tail fins pitched for helicopter mode (for autorotation), then dump the collective (feather) to an airplane-mode position for the wings and tail fins, pull out of the dive and glide before pushing over and pitching the wings and tail

fins back into their previous helicopter mode positions and land, as shown in Figure 10. The ardupilot [8] was used for data logging and a simple mathematical model for computation of rotor speed in helicopter autorotation mode was used [1].

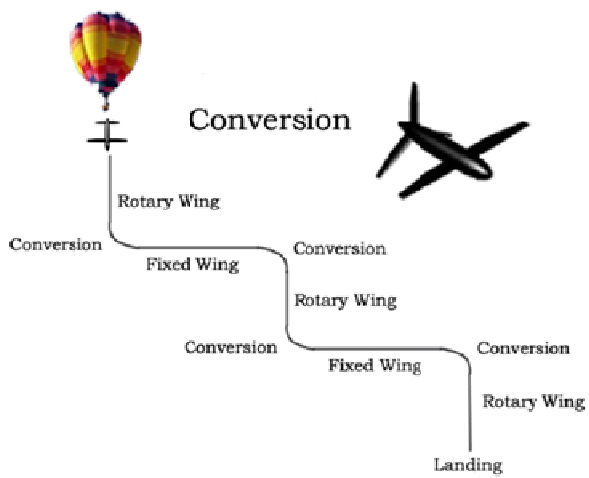

Figure 10: Stop-Rotor Big-Drop Test.

It should be noted that the big drop was unpowered and that the expression for rotor speed in autorotation can be directly used to compute rotor RPM and velocity [1]. Thus, from Drier [1], the first-order equation for rotor speed was assumed to be

$$\mathbf{J}\dot{\Omega} = \mathbf{Q}_{eng} - \mathbf{Q}_{rotor} \qquad (6)$$

where $\mathbf{J}$ is the inertia, $\dot{\Omega}$ is the angular velocity, and $\mathbf{Q}_{eng}, \mathbf{Q}_{rotor}$ are the engine torque and the rotor torque, respectively. The rotor torque, $\mathbf{Q}_{rotor}$, and thrust, $\mathbf{T}$, can be modeled as

$$\mathbf{Q}_{rotor} = \left(\frac{\Omega}{\Omega_0}\right)^2 \mathbf{Q}_0 \qquad (7)$$

$$\mathbf{T} = \left(\frac{\Omega}{\Omega_0}\right)^2 \mathbf{W} \qquad (8)$$

where Ω_0 is the initial speed and $\mathbf{W}$ is the weight. During the unpowered big drop, engine torque $\mathbf{Q}_{eng} = 0$ and the rotor speed equation is given by

$$\mathbf{J}\dot{\Omega} = -\left(\frac{\Omega}{\Omega_0}\right)^2 \mathbf{Q}_0 \qquad (9)$$

This is called Bernoulli's equation with the closed form solution

$$\Omega(t) = \frac{\Omega_0}{1 + \frac{\mathbf{Q}_0 t}{\mathbf{J}\Omega_0}} \qquad (10)$$

The equation of vertical motion during the big drop (i.e., free fall) is given by

$$\ddot{y} = g(1 - \frac{\mathbf{T}}{\mathbf{W}}) = g[1 - \left(\frac{\Omega}{\Omega_0}\right)^2] \qquad (11)$$

Equation (10) is substituted into Equation (11) and integrated numerically once for velocity $\dot{y}$ and twice for position y determination. The simulation results by numerically integrating dynamic equations of motion; the experimental results are shown in Figure 11. It should also be noted that initially from time t=2 seconds, when the stop-rotor device is in the autorotation mode, results are comparable. However, the difference between experimental RPM and simulation RPM increases as the time increases. The difference between simulation and experimental results can be attributed to approximate aerodynamic modeling, approximate mathematical model for the stop-rotor, inability to specify exact initial conditions during conversion and numerical integration error.

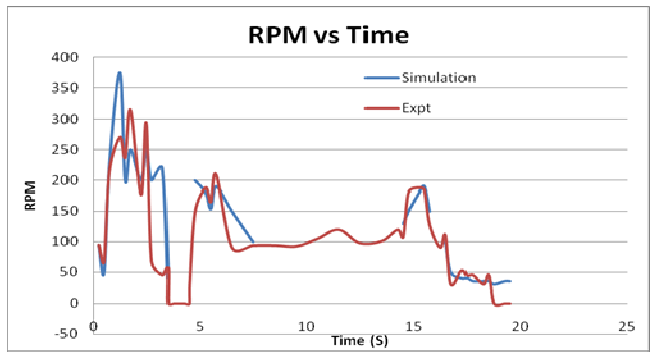

Figure 11: Comparison of simulation and experimental results

It can further be noted that during the drop from time t= 7 to14 seconds, the stop-rotor vehicle has undergone an uncontrolled roll in the fixed-wing mode that results into the discontinuity in simulation RPM from time t=7 to14 seconds (see Figure 12).

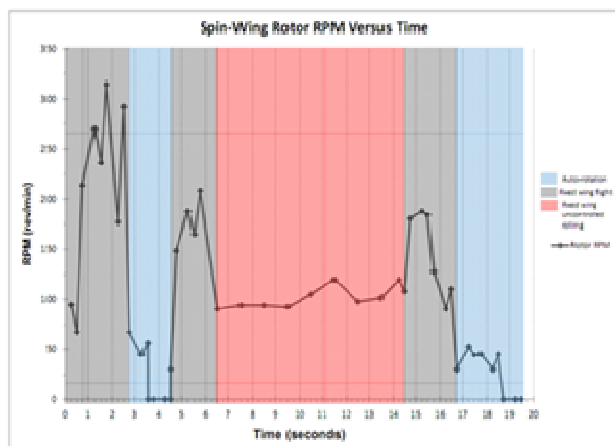

Figure 12. Stop-Rotor Flight Modes During the Big Drop

Conclusion

In this work, modeling, analysis and drop-test results on a novel stop-rotor UAV is presented. A low-cost, open-source autopilot was used in a data-logging mode to acquire flight data. The results from a simple mathematical model of the drop test were compared with the experimental data. A successful helicopter–to-fixed-wing-flight conversion was demonstrated during the drop test. Currently, researchers at ASU are working on modifying modeling and simulation to yield more accurate fidelity with measurements.

References

[1] M. Drier, Introduction to Helicopter and Tiltrotor Flight Simulation Published by AIAA, 2007, 1st Edition, ISBN-10: 1-56347-873-0, ISBN-13: 978-1-56347-873-4

[2] Kendoul, F. Fantoni, I. Lozano, R. "Modeling and Control of a Small Autonomous Aircraft Having Two Tilting Rotors"Robotics, IEEE Transactions on Volume: 22 Issue: 6, Dec. 2006 pp 1297 - 1302 ,

[3] Ghiringhelli G.L; Masarati P.; Mantegazza P; Nixon M.W. " Multi-Body Analysis of a Tiltrotor Configuration", Nonlinear Dynamics, Volume 19, Number 4, August 1999 , pp. 333-357(25)

[4] Vargas-Clara, "Finite Element Analysis of Stop-rotor" Class Project Report, Spring 10.

[5] http://xflr5.sourceforge.net/xflr5.htm Retrieved on 3/15/2011

[6] www.solidworks.com Retrieved on 3/15/2011

[7] www.Siemens.com/NX Retrieved on 3/15/2011

[8] http://www.pololu.com/catalog/product/1393 Retrieved on 3/15/2011

[9] http://diydrones.com/notes/ArduPilot Retrieved on 3/15/2011

Biographies

ALVARO VARGAS-CLARA, Alvaro Vargas-Clara is a graduate student in the Department of Engineering Technology at ASU Poly. He can be reached at vargasc@asu.edu

SANGRAM REDKAR, Sangram Redkar is an assistant professor in the Department of Engineering Technology at ASU Poly. His research interests include inertial measurement, MEMS dynamics, control, and nonlinear dynamics. He can be reached at sredkar@asu.edu.

Acknowledgements

The financial support from the US Navy is gratefully acknowledged.